An Electrical Rectifier Based on Au Nanoparticle Array Fabricated Using Direct-Write Electron Beam Lithography

*Boya Radha and Giridhar U. Kulkarni**

Close-packed arrays of Au nanoparticles are produced in patterned regions by electron beam (e-beam) lithography using a highly sensitive direct–write resist, $N^+AuCl_4^-(C_8H_{17})_4Br$. While the e–beam causes dewetting of the resist to nucleate Au nanoparticles, the following step of thermolysis aids particle growth and removal of the organic part. Thus formed arrays contain Au nanoparticles. Such arrays are patterned into ≈10 μm wide stripes between Au contact pads on SiO_2/Si substrates to realize electrical rectification. Under forward bias, the device exhibits a threshold voltage of +4.3 V and a high current rectification ratio of 3×10^5, which are stable over many repetitive measurements. The threshold voltage of the rectifier can be reduced by applying an electric stress or by varying the electron dosage used for array formation. The nanoparticle rectifier element could be transferred onto flexible substrates such as PDMS, where the nanoparticle coupling is influenced by swelling of the substrate. Obviously, the nanoparticle size, shape, and the spacing in array are all important for the rectifier device performance. Based on the electrical measurements the mechanism of rectification is found to be due to switching of electrical conduction with applied bias, from short–distance tunneling to F–N type tunneling followed by transient filament formation.

1. Introduction

The method of rectifying an alternating current is historically perhaps the first step towards electronics. The evolution of this tiny circuit element, namely a diode, has seen several generations starting from vacuum tubes to semiconductor p–n junctions.[1] During the last decade, since the advent of nanotechnology, several nanomaterials have been tried out for diode action. These include ZnO nanowires,[2] carbon nanotubes (CNT),[3] graphene,[4] tailored donor–acceptor molecules,[5] nanoparticle–polymer composites,[6] etc. These devices essentially rely on asymmetric junction formation at the nanomaterial–electrode interface[7] or a junction formed within the nanomaterial due to differential doping.[2] In addition, nanoparticle arrays[8] particularly of Au and Ag, stabilized by organic spacers have been employed for electrical rectification.[9–11] In contrast to the colloidal state, metal nanoparticles assembled onto a substrate as an ordered array represent a quasi-2D system where the interparticle coupling,[12] depending on its strength, can give rise to collective properties[13] unique to the nanoparticle organization.[14] The interparticle coupling is tuned[15] by suitably choosing the linker molecule[11] or by dynamically changing its length or conjugation.[16,17] While the nanoparticle arrays can be directly contacted by laying metal electrode pads,[11] the use of scanning probe methods is not uncommon.[10,18] Electrical rectification is one among the range of interesting properties in metal nanoparticle arrays, other important properties being the metal–insulator transition,[19] magnetic transitions,[20] single electron tunneling,[21] linear and non–linear optical response,[22] and, more recently, acoustic rectification.[23] A list of metal nanoparticle based electrical rectifiers is presented in Table S1 (Supporting Information). Making a stand alone nanoparticle device reproducible both in fabrication and performance is, indeed, a herculean task and this has been achieved in this work in a simple and elegant way.

A survey of the literature shows that the nanoparticle arrays are usually obtained by the self–assembly methods[24–26] by drop-drying the nanoparticle dispersion[25] on a desired substrate or at air–water interface using the Langmuir–Blodgett method.[22] Instead of 2D, Au nanoparticle wire arrays have been fabricated by convective self-assembly method with tunable conductivity.[27] Recently, inkjet printing has been employed to produce Au nanoparticle arrays which work as immunosensors.[28] Micromolding nanoparticle superlattices has also been demonstrated.[29,30] Dip-pen lithography has been used to draw Au nanoparticle lines.[31] Extended arrays have been produced using nanosphere lithography,[32] diblock copolymer micelles,[33] etc. In this context, direct-write techniques are becoming popular as they cut down the number of process steps and provide a better control on the nanomaterial property.[34] For direct write ion or electron beam lithography (EBL), various metal–organic precursors have been explored as negative resists, the notable ones for Au being Au(I) thiolate thin films[35] and Au loaded block copolymer micelles.[36] These methods have led to patterning Au nanoparticles into regular extended arrays. However, the

B. Radha, Prof. G. U. Kulkarni
Chemistry and Physics of Materials Unit
and DST Unit on Nanoscience
Jawaharlal Nehru Centre for
Advanced Scientific Research
Jakkur P.O., Bangalore 560064, India
E-mail: kulkarni@jncasr.ac.in

DOI: 10.1002/adfm.201103170

obtained nanoparticle arrays have not been reported to show any rectifying action.

Here we report, a highly versatile, single-step direct write EBL process employing a single source precursor wherein the nucleation and growth of Au nanoparticles into close packed arrays takes place in confined boundaries defined by patterning. In particular, we have fabricated micron wide stripes of Au nanoparticle (size ≈ 25 nm) arrays, which exhibit electrical rectifier action with high rectification ratio. This is for the first time, a metal nanoparticle rectifier with highly commendable characteristics has been developed. In addition, we demonstrate the transferability of the patterned arrays onto a polymer substrate, where the latter could undergo swelling and deswelling causing variation of inter-nanoparticle spacing and hence the electrical transport.

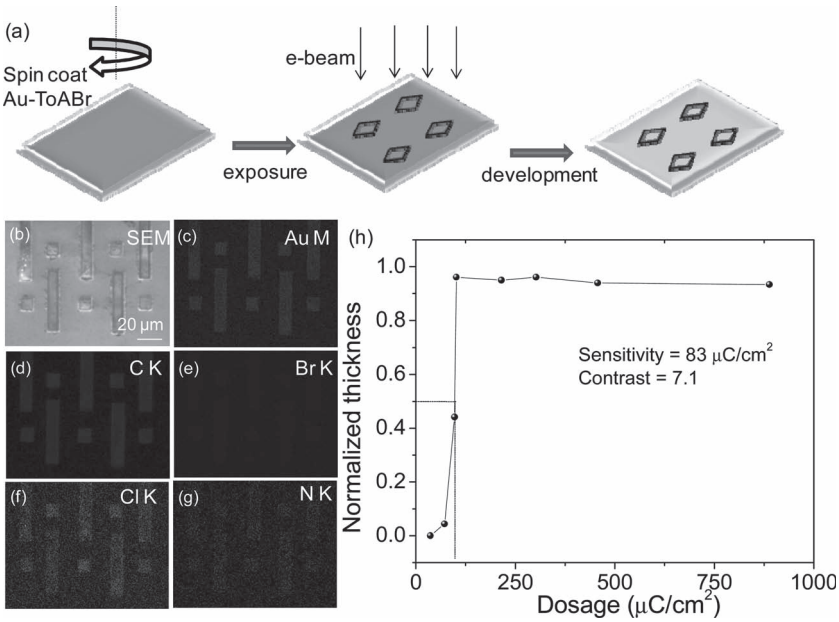

Figure 1. Au–ToABr e-beam resist: a) Schematic of EBL using Au–ToABr direct–write resist: spincoating, e-beam exposure, and development in toluene for 10 s. b) Scanning electron microscopy (SEM) image of patterned Au–ToABr e–resist and c–g) the corresponding EDS maps. h) Variation in the film thickness (after development) of Au–ToABr normalized with respect to initial thickness, versus the e-dose (beam energy, 5 kV).

2. Results and Discussion

2.1. Direct-Write Resist Action and Nanoparticle Array Formation

Recently, we reported, a generic way of producing patterns of various materials including Au, by direct writing methods.[37] Interestingly under the given conditions, Au formed nanoparticulates whereas most other metals appeared as continuous features. In that report, the inherent response of the Au resist to the electron beam (e-beam) exposure was left unattended. We considered it worth investigating in detail the e-beam resist action of the Au precursor. The e-beam resist used is $(AuCl_4)^-$ anions phase transferred using ToABr, i.e., $N^+AuCl_4^-(C_8H_{17})_4Br$ (henceforth termed as Au–ToABr). Au–ToABr forms smooth films (roughness, 3.4 nm, see Supporting Information Figure S1) by spin coating. The direct-write EBL process with Au–ToABr resist is simple, as illustrated in the schematic in **Figure 1**a. Patterning of Au–ToABr film has been carried out under varying e-beam dosages, an example obtained using a 5 kV e-beam at 95 μC cm^{-2} is shown in Figure 1b. The regions exposed to the e-beam remained on the substrate after developing in toluene, thus indicating the negative-tone resist behavior of Au–ToABr. EDS images of a typical patterned region (shown in Figure 1c–g), as expected, indicate the presence of C, Br, and Cl, along with that of Au in the designated areas. The Au/Cl/Br/C elemental ratios (20:11:7:62) obtained for the patterned regions agree with the initial composition (19:10:8:63) of the unexposed resist, implying that the electron dosage (e-dosage) and developing cause only minimal change in the overall composition. Small differences seen can occur due to carbon contamination during the e-beam exposure. Importantly, the resist action of Au–ToABr is evident. This is also reflected in the UV–visible absorption spectrum (Figure S2a, Suppoarting Information) where the characteristic features of the Au–ToABr complex disappeared. The crystalline pristine complex tends to become amorphous after the e-beam exposure as seen in the X-ray diffraction data (Figure S2b, Supporting Information). In order to quantify the resist action, squares of 10 × 10 μm^2 were patterned on a Au–ToABr film while gradually increasing the e-dosage from 35 to 800 μC cm^{-2} on different areas (beam energy, 5 kV and beam current, 2.9 nA). The threshold dosage for the resist action was 64 μC cm^{-2} below which the developed regions failed to exhibit a contrast. The thickness of the developed region as measured using optical profilometry increased with the e-dosage, from ≈7 nm at 64 μC cm^{-2} to ≈160 nm at 800 μC cm^{-2} clearly due to the increasing resist action (Figure 1h). In other words, at the minimum dosage value, only about 4.4% of the original thickness is retained following developing in toluene, and this value gradually increased to 95% beyond 90 μC cm^{-2}. The sensitivity value for Au–ToABr resist is 83 μC cm^{-2}, which compared to other direct write resists, is commendable. The e-dosage employed here is far lower than the typical values reported for Au direct write precursors, e.g., 1.5 mC cm^{-2} for Au nanoparticle resist,[38] 0.2 mC cm^{-2} for Au–polymer composite[39] and 0.5 mC cm^{-2} for Au(I)–thiolate.[35] The measured contrast value for Au–ToABr resist was 7.1 (see Figure 1h). Generally, a higher contrast implies possibility of high-resolution patterning with the resist.[40]

The advantage of a direct write resist is its ability to produce active material with fewer processing steps. Indeed, a simple thermolysis of Au–ToABr film (300 °C, 3 h) removes the organic part and leaves behind only the crystalline Au metal. In the thermogravimetric analysis (TGA) curve in Figure S3 (Supporting Information), the residue of 29% corresponds to metallic Au. EDS map of the thermolyzed patterns show the presence of Au in patterned regions with negligible amount of carbon

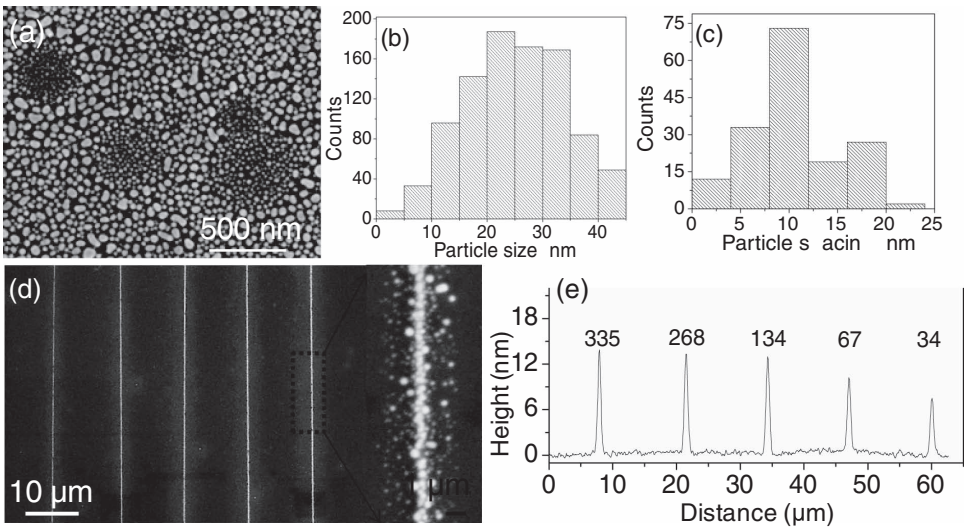

Figure 2. a) SEM image of a Au–ToABr film exposed to e-beam (100 µC cm^{-2}), developed and thermolysed at 300 °C, showing tightly packed Au nanoparticles, along with histograms of particle size (b) and spacing (c). d) SEM image of the patterned Au nanoparticle lines with a magnified view in the inset. e) Height profile of the lines, with the dosages indicated in µC cm^{-1}.

(see Figure S4, Supporting Information). To further confirm, we performed Raman measurements (Figure S5, Supporting Information). The pristine Au–ToABr precursor does not possess any peaks in the region of interest (1000–2000 cm^{-1}). After exposure to e-beam, two broad peaks corresponding to D (1360 cm^{-1}) and G (1584 cm^{-1})[41] appeared indicating carbonization of the precursor under the e-beam. Following thermolysis, the peaks disappeared implying complete removal of the amorphous carbon (formed from the precursor). Accordingly, the X-ray diffraction pattern of a thermolysed film showed peaks from Au (see Figure S6, Supporting Information). When not exposed to e-beam, the metal product resulting from thermolysis may contain interesting structures instead of a featureless smooth film; in our previous study[42] we have been able to nucleate and grow large plate-like polygonal Au structures starting with the Au–ToABr complex by fine-tuning the thermolysis conditions. However, a e-beam exposed film behaved very differently following thermolysis at 300 °C (**Figure 2**). Upon thermolysis of the e-beam exposed Au–ToABr resist, fine Au particulates were obtained as shown in Figure 2a. We see somewhat non-spherical nanoparticles in the size range of ≈5 to 40 nm packed in a roughly hexagonal array. The mean particle size was found to be ≈25 nm (Figure 2b), and the mean spacing, ≈10 nm (Figure 2c). Interestingly, we observe 100 to 800 nm wide circular regions in Figure 2a, in which the nanoparticles are rather small (2–20 nm) and more tightly packed. This aspect will be dealt later. As examples of high-resolution patterning, parallel lines of decreasing widths (minimum width ≈70 nm) were produced as shown in Figure 2d. The height profiles of the same in Figure 2e indicate a remarkable control on nanoparticle line thickness based on the e-dosage.

The direct resist action producing nanoparticle arrays is indeed intriguing and therefore, we have investigated this aspect in some detail which is summarised in the schematic in **Figure 3**a. When observed during the e-beam exposure, the pristine Au–ToABr resist film seemed to dewet leading to dark features, which with increasing time of exposure, were finely distributed all over (see Movie S1, Supporting Information). As these features bear a darker contrast, they may predominantly contain organic species from the resist. SEM image in Figure 3b shows that the dewetted features have extension in the range of ≈0.05 to ≈1.3 µm. An atomic force microscopy (AFM) topography image (Figure 3c) of the features showed that they are indeed protrusions, with a mean height of ≈7.7 nm (Figure 3d) and mean width of ≈0.48 µm (Figure 3e). When this film was developed in toluene (10 s) and examined in SEM, the dark blobs (being organic) were almost washed away (Figure 3g). Instead, tiny Au nanoparticles were seen all over, i.e., in dark (Figure 3f) as well as in gray (Figure 3h) regions. From this experiment, it is clear that e-beam induces nanoparticle nucleation (see schematic illustration in Figure 3a). Electrostatic interactions between the $(AuCl_4)^-$anions and ToABr perhaps enables easy liberation of Au upon mild e-beam exposures. Due to e-beam induced dewetting of the resist, only Au nanoparticles are obtained and not extended features. Although Figure 3 is an illustration for dewetting on a larger scale, most blobs were tiny (<100 nm) as evident in the histogram in Figure 3e where the mean value is at ≈0.48 µm. It therefore appears plausible that the film dewets in nanometer regions, which following thermolysis leads to individual Au nanoparticles. During the thermolysis, the nanoparticles are allowed to grow with the supply of Au^{3+} from the precursor available around, except in those regions, from which blobs got formed and washed away. This accounts for the occurrence of circular regions containing relatively smaller nanoparticles as shown in Figure 2a.

E-beam induced heating of organic/polymeric resists is well-known and discussed in the literature. Thermally activated effects are important and in the case of organic resists, it has been simulated and experimentally verified that thermal effects lead to distortion of the patterns.[43] For instance, in the case

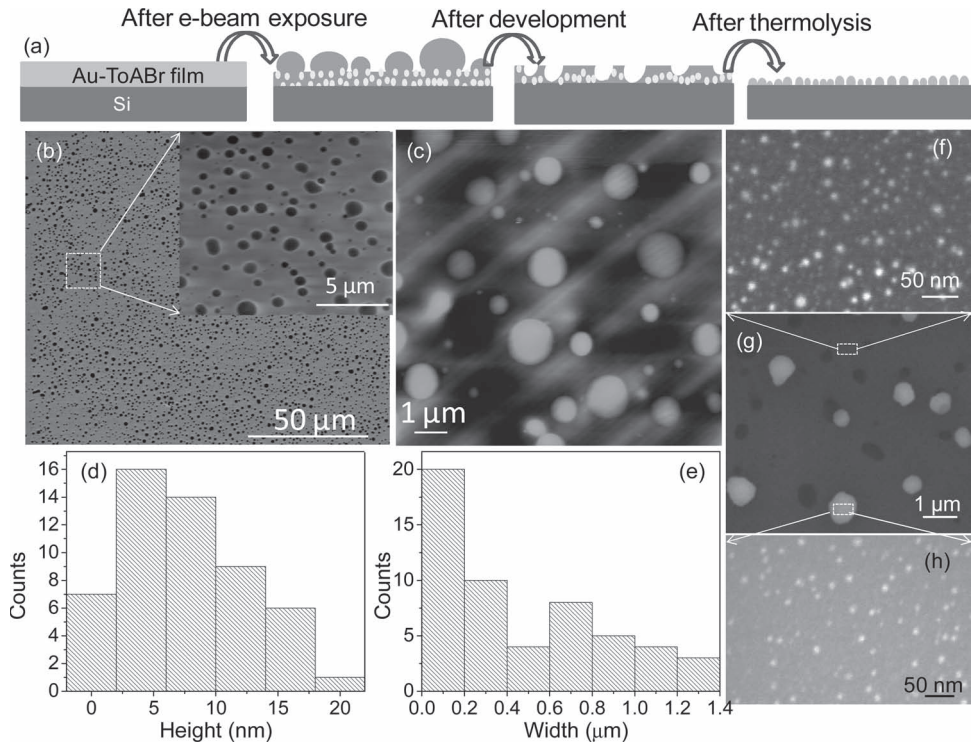

Figure 3. a) Schematic showing the e–beam induced dewetting of the Au–ToABr spincoated resist on a Si substrate; dots represent Au nanoparticles. b) SEM and c) AFM images of a Au–ToABr film (≈150 nm thick) exposed to the e-beam (0.5 mC cm^{-2}) showing the e-beam induced dewetting. Magnified image is shown in the inset of b. d,e) Histograms of the height and width of the blobs based on AFM. g) SEM image after development and prior to thermolysis. Bright spots seen all over, correspond to the Si regions exposed as the blobs got washed off. Magnified portions of the dark (f) and bright (h) regions both show the presence of reduced Au nanoparticles.

of PMMA (at 20 kV, 20 μC cm^{-2}), temperatures up to 200 °C have been calculated.[44] This was an analytical model taking into account the beam current and the substrate. If the substrate is a poor thermal conductor, it takes time to dissipate the heat and thermal effects on the resist would be significant. In our resist i.e., Au-ToABr resist, e-beam induced heating can be expected as well. Exposure to e-beam induces dewetting due to local heating of the resist, much the same way polymeric resists behave. As the thermal conductivity of the substrate used (Si) is high (149 W m^{-1} K^{-1}),[45] it should act as an infinitesimal heat sink thus avoiding the pattern distortion to some extent. As such, when a spin coated film of Au-ToABr is heated on a hot plate at 50 °C, thermal dewetting occurred and the film was found to split into blob kind of structures as seen under optical microscope (Figure S7a, Supporting Information). This was in the absence of e-beam. These are much larger than the ones observed with e-beam induced dewetting (see Figure 3). With both e-beam and external heating on, the latter had pronounced effect at large length scales leading to a situation similar to thermal dewetting (Figure S7b, Supporting Information), as though e-beam had no effect. However, at higher magnifications, Au nanoparticle formation was seen restricted to dewetted regions. This is not a desired situation for device fabrication as regions in between the blobs were devoid of nanoparticles. With e-beam (alone) induced spinodal dewetting (Figure S8, Supporting Information), continuous arrays of nanoparticles can be formed as the e-beam seems to produce only local heating. The spinodal dewetting has been observed in thin metal film (≈5–30 nm) when exposed to e-beam (30 kV, 54–82 μA) to lead to nanoparticles.[46] On the other hand, in the case of liquid crystal and liquid metal films also,[47] such dewetting has been observed. Since Au-ToABr shows liquid crystalline nature and undergoes spinodal dewetting (see Figure S8, Supporting Information), the scenario may be similar to dewetting of the liquid. All the above findings point out that unlike chemically organized assemblies, in this recipe no external capping agent is required for nanoparticle array stabilization. On the contrary, the organic part of the resist gets removed during the thermolysis step. The organization of nanoparticles in arrays takes place spontaneously due to e-beam induced dewetting of the resist at different length scales followed by particle nucleation and growth.

2.2. Au Nanoparticle Array as a Half-Wave Rectifier

For the purpose of constructing a two–terminal device, Au nanoparticle array stripes were defined by EBL in between a pair of Au contact pads (see optical image with rectifier electrical connections indicated, as the inset of **Figure 4**a) and the current–voltage (*I*–*V*) characteristics were measured. The current was low initially (≈0.4 nA) and a sharp rise was observed beyond

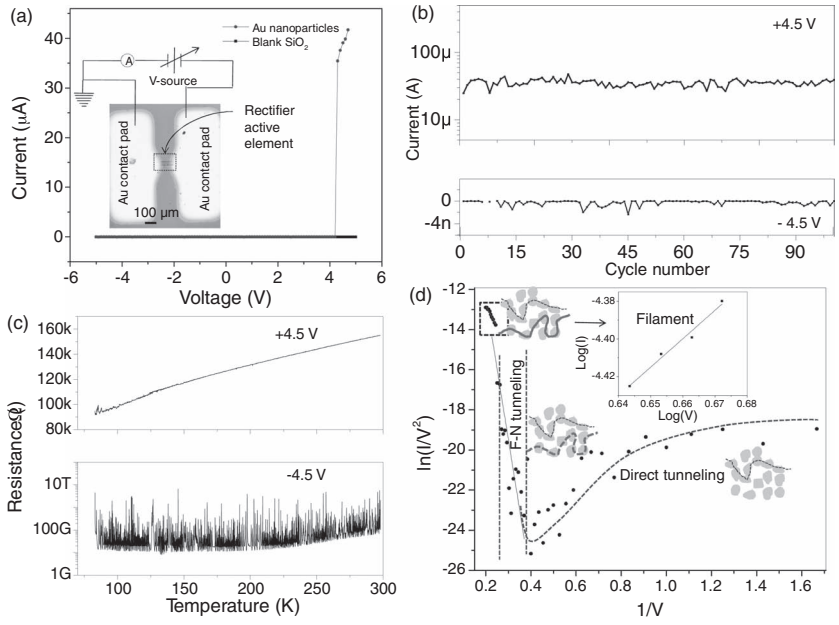

Figure 4. a) Two probe *I–V* characteristics of the Au nanoparticle array stripes patterned by direct–write EBL (red, e-dosage ≈783 μC cm^2) on a SiO_2 (300 nm)/Si substrate along with that from the blank substrate (black). Inset shows an optical image of the device along with the schematic of the circuit. b) Switching the applied voltage, +4.5 V and –4.5 V, in cycles and monitoring the current. c) Low temperature resistance measurements on the rectifying device performed at +4.5 V and –4.5 V. d) A F–N plot of the Au nanoparticle rectifier. Three regions, namely direct tunneling, F–N tunneling and filament mode of conduction are marked and schematics of conduction are shown along with. Inset shows log (*I*) vs log (*V*) plot above the threshold voltage.

a forward voltage of +4.3 V, while in the negative bias region, the current remained at fraction of a nA up to –5 V for this device. The current rectification ratio, which is the ratio of forward to reverse currents at a given bias, is estimated to be ≈3 × 10^5 (at ± 4.5 V), which is considerably higher than the reported values from nanoparticle arrays.[10,11] The device characteristics are highly stable and reproducible both in fabrication and performance (see characteristics of the second device in Figure S9, Supporting Information). Some devices showed rectification in the negative bias region and others, in the positive bias region; of course, this observation is only relative as the choice of electrode polarity, positive or negative, is simply arbitrary (vide infra). Another device (third one) was tested by cycling between +4.5 V and –4.5 V continuously (Figure 4b). Over the observed 100 cycles, the rectifier action was well preserved, with the positive bias (+4.5 V) current being much higher than that at the negative bias (–4.5 V). Low temperature resistance measurements have been carried out on the rectifier device in order to understand the nature of the conducting and insulating states. When the device resistance was measured applying +4.5 V, the resistance decreased with decreasing temperature (see Figure 4c), resembling metallic behavior. On the other hand, the device resistance remained almost independent of temperature, when measured at –4.5 V (Figure 4c).

Various reports in the literature have described rectification involving nanoparticles as due to different widths of the tunnel barriers on either sides of the nanoparticles[10] or due to asymmetric coupling of the nanoparticles at the electrode interfaces.[48] Where some slight movements are possible such as in Langmuir monolayers, collective realignment of the nanoparticle dipoles can lead to current rectification.[11] In the nanoparticle devices presented here, the direct-write EBL process produces well separated nanoparticles (see SEM image in Figure 2a) with no possibility of direct contact between the nanoparticles. As the electrodes are identical and the spacer molecules are practically absent, one cannot invoke rectification mechanisms relying on electrode or spacer induced asymmetries. Besides, the observed high rectification ratio of 10^5 cannot be expected from such asymmetries alone.[49] We feel that there are other mechanisms at play.

In the present device at negative or near zero bias, the conduction may rely on paths where the interparticle separations are of the order of ≈1 nm, suitable for tunneling, leading to the low current region. As the conduction is due to tunneling, the resistance is nearly independent of temperature under such bias conditions (Figure 4c, at –4.5 V). The unsymmetrical nature of the *I–V* characteristics and the anisotropic shape of the nanoparticles along with the large interparticle spacings (1–25 nm) prompted us to think that besides direct tunneling, there must exist a Fowler–Nordheim (F–N) type polarity dependent tunneling. This is corroborated by the F–N plot shown in Figure 4d, the shape of which owes much to the changing shape of the tunnel barrier under varying bias.[50,51] We have distinctly identified three regions in bias dependent characteristics: direct tunneling (up to ~≈.5 V), F–N tunneling (≈2.5 to ≈4.2 V), and transient filament formation due to field induced electromigration (≥4.3 V). Although the particle asymmetry is not along any particular direction, under the electric field, percolative paths set in and link only the relevant nanoparticles, thus bringing in an unintentional asymmetry, for which the contact electrodes (being identical) have little role to play. The percolative path of F–N tunneling may involve sharp corners and rounded surfaces of the nanoparticles from one electrode to the other, the direction of easy flow of current (forward path) being along the path (see schematic diagrams in Figure 4d). The F–N tunneling equation is written as[51]

$$\ln\left(\frac{1}{V^2}\right) = \ln\left(\frac{\alpha A(\beta^2/\phi)}{d^2}\right) - \frac{Bd\phi^{3/2}}{\beta}\ \frac{1}{V} \quad (1)$$

where I is the current; α is the emission area; V is the voltage (≈2.5 V to ≈4.2 V); d is the distance between the electrodes (≈92 μm); ϕ is the work function of gold (5.1 eV); A and B are the constants given by 1.56 × 10^{-10} AV^{-2} eV and 6.83 × 10^3 V eV$^{-3/2}$ μm^{-1}, respectively; and β is the field enhancement factor. A plot of $\ln(I/V^2)$ versus $(1/V)$ is linear in the range, 2.5 V to 4.2 V (see Figure 4d), the slope of which gave $\beta \approx 10^5$. In F–N tunneling involving metal nanostructures, such high values for β may be expected.[52,53]

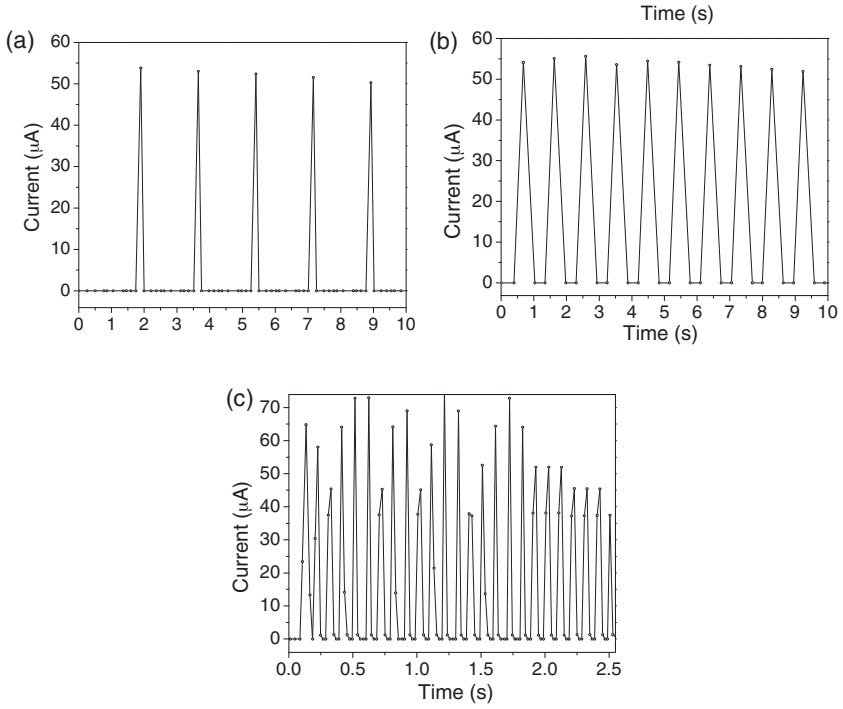

Figure 5. Rectification at different frequencies: current vs time curves at a fixed applied voltage of 4.5 V for sine wave of frequencies of a) 0.5 Hz, b) 1 Hz, and c) 10 Hz.

As the voltage is increased beyond 4.2 V, an additional mode of conduction by filament formation is possible. Such filaments may get formed due to electromigration as the electrical stress from the applied voltage can induce slight changes in the alignments of the nanoparticles or in the particle shape,[11,54] with some contribution from joule heating as well. A plot of log (*I*) versus log (*V*) for the voltage range, 4.3 to 4.7 V, is found to be linear with a slope close to 1 (≈1.3) indicating ohmic conduction[55] (see inset in Figure 4d). The low temperature measurement shown in Figure 4c for $V = +4.5$ V also confirms the metallic behavior. Only filament formation can account for the observed colossal increase in current to few μA. However, these filaments are not permanent contacts as no such features were seen in the SEM image of the device after operation (see Figure S10, Supporting Information). The fact that the current diminishes to less than few nA once the voltage is withdrawn (or opposite bias is applied), itself implies that these filaments are transient, present only under high bias condition. As the width of the nanoparticle array is limited to few μms, one cannot also expect many such filaments, thus limiting the diode action to perhaps only one or just few. Whether one or few paths, they ought to be unidirectional to bring in the desired asymmetry, which also means that paths in the opposite direction cannot be favored. This is essentially a morphology controlled device. Among the fabricated devices, some show rectification at positive bias voltages, while others on the negative bias; however this observation may not be of much significance as the electrode polarity is arbitrary as noted earlier.

We have studied the rectifier action for different sine wave frequencies (**Figure 5**). At lower frequencies, 0.5 and 1 Hz (Figure 5a,b, respectively), the half-wave rectification was quite convincing, while at 10 Hz, small variations were seen in the forward bias current value. At higher frequencies (100 Hz or above), the device did not show a good response (not shown). Here, we compare the performance of our device with the literature reports on nanomaterial based rectifier systems, specifically the stand-alone devices, which do not make use of other equipment such as scanning probe microscopes (Table S2, Supporting Information). Compared to most devices listed in Table S2 (Supporting Information), the present device has relatively high threshold voltage, current, and rectification ratio, comparable to a CNT device.[3] Unlike the case of CNT based diodes, fabricating the active element and establishing electrical contacts with this device is rather straight forward.

Tunability of the low-current region is an additional advantage with the present nanoparticle array rectifier. The *I*–*V* sweeps between ±5 V obtained after intermittently applying electrical stress at 8 V show that the low-current region can be made to shrink. From the magnified view in **Figure 6**a, we see that the shrinkage is rather sudden after the first and second stress and becomes gradual thereafter, which is quantitatively shown in Figure 6b. By applying a stress of 15 V, the *I*–*V* data was made close to linear. The shrinkage of the low-current region and increase in the forward current imply increased physical connectivity between the nanoparticles, involving permanent filament formation along the nanoparticle chain induced electrically. This observation further corroborates the mechanism of rectification explained earlier. We also employed the e-dosage as a tool to vary the nanoparticle size, spacing, and thus the threshold voltage of the rectifier. At a lower e-dosage i.e., 78 μC cm^{-2}, smaller nanoparticles (mean size, ≈19 nm) with lesser spacing were obtained (Figure 6c). The *I*–*V* curve showed a threshold voltage of 2.2 V (Figure 6d). At a much higher e-dosage (1566 μC cm^{-2}), the rectification was lost (Figure S11, Supporting Information).

In order to understand the effect of line width of the Au nanoparticle array on the rectifier characteristics, a systematic study was performed with different line widths of the nanoparticle rectifier stripes i.e., 2, 5, 15, 30, and 60 μm (in addition to 10 μm). As the width of the array increased, the threshold voltage decreased (Figure 6e,f). For instance, in the case of 60 μm, the rectifier characteristics showed a threshold voltage of ≈0.5 V, much lower than that seen in the case of 10 μm stripes (≈4.3 V). The increased width of the rectifier element thus leads to more F–N tunnel paths. Concomitantly, the current also increased considerably (see Figure 6e and Figure S12, Supporting Information). The variation of threshold voltage exhibits a smooth trend with the line width (Figure 6f). On the other hand, with the line width of 2 μm, the threshold voltage is beyond 12 V and the forward current is also less. The other important observation is that the reverse current increases with

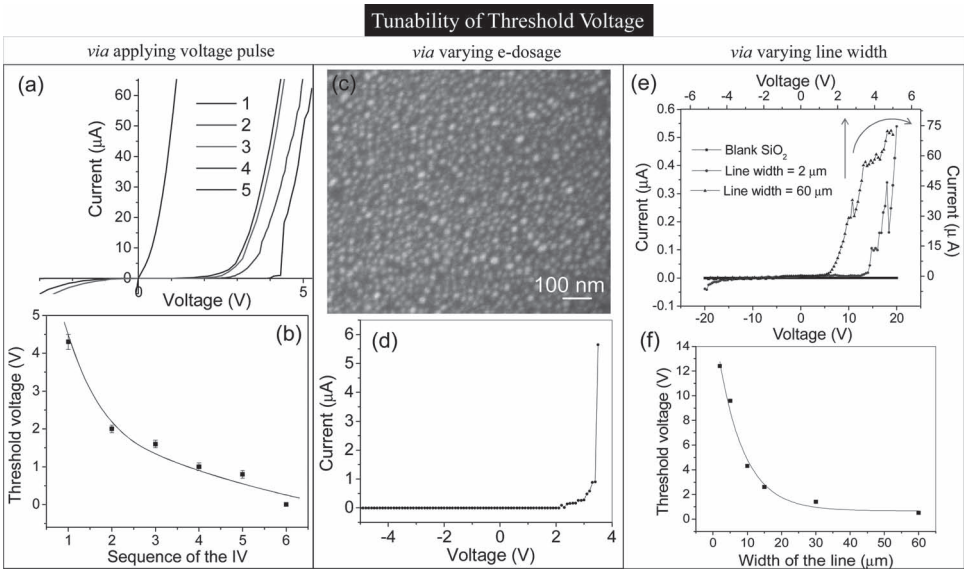

Figure 6. Tunability of threshold voltage. a) Sequential *I–V* characteristics from –5V to +5V. After each sweep, an electrical stress of 8 V was applied. The low-current region being shrunk as higher voltages are applied. *I–V* characteristics named 5 was obtained after stressing with 15 V. b) The threshold voltage of the rectifier device for the successive sweeps plotted vs sweep number (the line drawn is only a guide to eye). A lower threshold voltage could also be obtained by varying the e-dosage use for Au nanoparticle array formation. c) SEM image of the Au nanoparticle array produced by e-dosage of 78 μC cm^{-2}. d) *I–V* characteristics of the resulting rectifier. e) *I–V* characteristics of rectifiers with varying line-widths of Au nanoparticle arrays. f) Threshold voltage versus line width of the nanoparticle array.

the line width, as expected due to increased direct tunneling paths (Figure S13, Supporting Information). Also, the current in the reverse bias increases with the decreasing threshold voltage. We observe good rectification at threshold voltages ≥1.5V (Figure S13, Supporting Information). A different contact scheme was attempted as well. Instead of Au, Ni metal was used for contacting the nanocrystal array. The diode action was repeatable with nearly similar characteristics (Figure S14, Supporting Information). This further strengthened our notion of Au nanoparticle based rectification.

We have transferred the Au nanoparticle array stripes (obtained with ≈783 μC cm^{-2}) to a flexible substrate i.e., poly(dimethylsiloxane) (PDMS). By masking the stripes on PDMS, Au deposition was done to define the contact pads (**Figure 7**a). Upon closely examining the stripes (inset in Figure 7b), we observe wrinkles on the PDMS surface which are a result of the PDMS shrinkage during curing.[56] This is expected to have some influence on the interparticle spacing. Although our efforts using SEM were unsuccessful because of surface charging of the substrate, there is enough evidence in the literature that PDMS shrinkage can cause a mismatch in the registry of the transferred patterns.[57] Thus, the *I–V* characteristics in Figure 7c, no longer shows a flat gap region near zero bias (compared with Figure 4a) but exhibits a finite slope extending on both sides of zero bias indicating that the conducting paths now involve nanoparticles in contact, though the contact may be very subtle. At a higher positive bias (approximately +3.1 V), however, the slope increased (Figure 7b) further pointing to a similar mechanism that prevails in devices hosted on SiO_2/Si substrates.

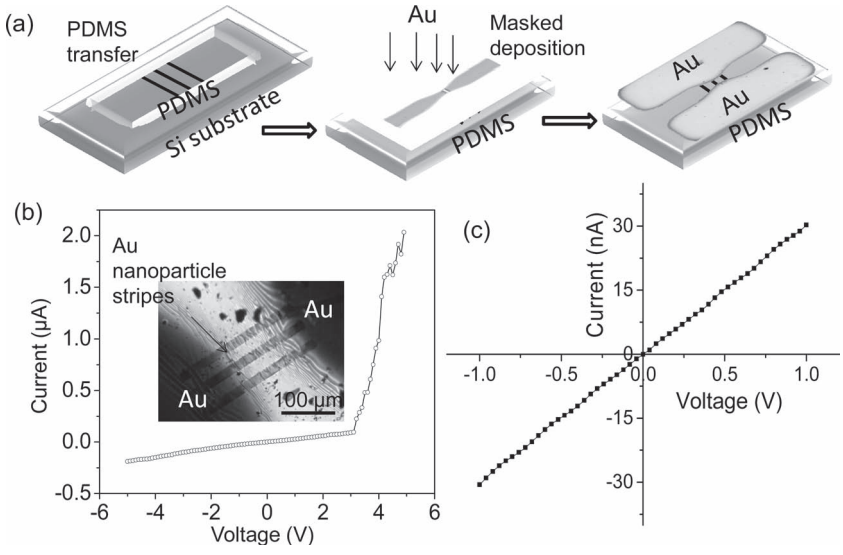

Figure 7. a) Schematic showing the transfer of patterned Au nanoparticles onto a PDMS substrate and masked deposition of Au contact pads. b) *I–V* characteristics of the device obtained in different voltage ranges. Optical image in the transmission mode of the obtained device is shown as inset. The wrinkles developed due to shrinkage of PDMS. c) *I–V* characteristics in the low bias region showing no blockade.

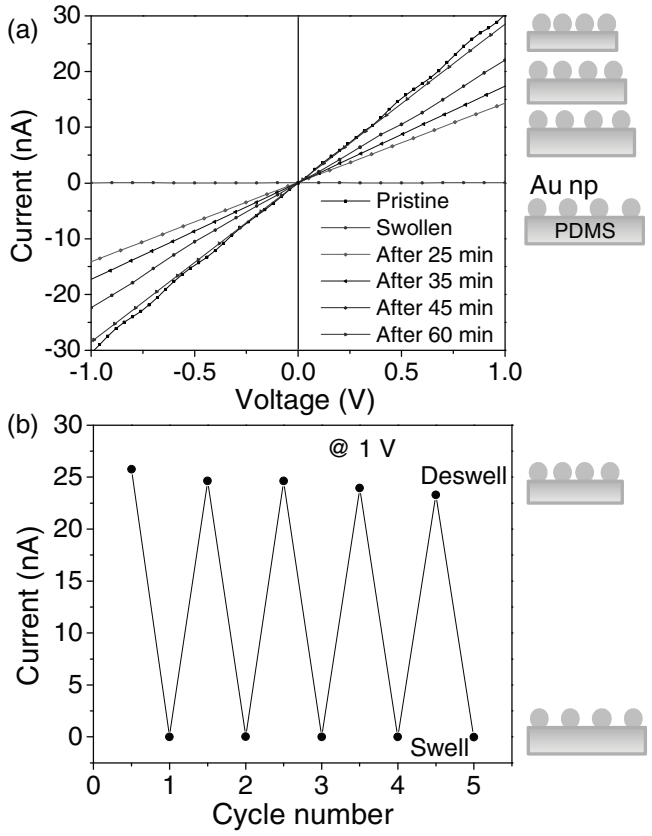

Figure 8. a) *I–V* characteristics collected during deswelling of toluene-treated PDMS carrying the rectifier device at different time intervals. b) Swell-deswell cycles monitored with the device. The schematic illustrations are shown alongside.

As PDMS is flexible, the nanoparticle contact can be manipulated (**Figure 8**). One simple way to do this is to swell PDMS by an organic solvent such as toluene.[58] A brief exposure to toluene brought down the current in the device to under 50 pA (Figure 8a), indicating that nanoparticle contacts along the conducting paths were weakened due to swelling of the substrate. Interestingly, the current in the device nearly regained as the substrate gradually put out toluene by evaporation (Figure 8a). We could reversibly swell and deswell the substrate in many cycles and observe the effect in *I–V* characteristics (Figure 8b). Finally, for specific applications, nanoparticle arrays can be made electrically continuous on chosen substrates by filling in interparticle regions with electroless deposition of Au (Figure S15, Supporting Information).

3. Conclusions

In conclusion, we have produced patterned regions of Au nanoparticle arrays with a reasonable control on particle size and spacing. This was achieved using direct-write e-beam lithography employing a Au–organic complex namely, $N^+AuCl_4^-(C_8H_{17})_4Br$, which was found to be highly sensitive (sensitivity, 83 μC cm^{-2}). The unique property of the resist is that upon e-beam exposure, it is found to dewet into nanosized blobs and reduce to Au nanoparticles, which upon thermal treatment at 300 °C in air, grow further getting rid of the organic part. The rectifier contains nanoparticles of different shapes with sharp corners and blunt surfaces, yet maintaining several nanometer wide spacing, a property which was exploited in fabricating a diode. Electrical transport measurements across patterned Au nanoparticle array stripes (≈10 μm wide) have shown rectification with a rectification ratio of 3×10^5 and the forward bias threshold voltage of +4.3 V. The threshold voltage can be tuned by applying higher voltage stress, by varying e-dosage or the line width. Tunability of the threshold voltage represents an important property of rectifier and is extremely useful for complementary logic circuits using nanoelectronics. The proposed mechanism of rectification is F–N tunneling, which leads to transient filament formation due to field induced electromigration at and above the threshold voltage. Low temperature measurements above threshold voltage have confirmed the metallic state of conduction. Finally, the device fabrication described in this article opens up many possibilities where the interparticle spacing as monitored through the tunnel current serves as a guiding factor for an application. We have demonstrated how swelling and deswelling of a PDMS substrate carrying the device and exposed to toluene can be monitored. The simplicity of this all-gold device fabrication by direct-write EBL is clearly an attraction.

4. Experimental Section

$HAuCl_4.3H_2O$ (49% Au) and and tetraoctylammonium bromide (ToABr) (98%) were obtained from Spectrochem; toluene from SD-fine chemicals and were used without further purification. The water used throughout this investigation was double distilled. The Au–ToABr e-resist was prepared by phase transferring $(AuCl_4)^-$ ions from an aqueous solution (50 mM) to ToABr in toluene (50 mM) as ToABr is a phase transfer agent.[59] The two-phase mixture was briskly stirred until all the $(AuCl_4)^-$ ions were transferred into the organic layer. As the phase transfer happens, the yellow colored bottom aqueous layer becomes colorless and the top organic layer develops red color which was separated. Si(100), Si/SiO_2 (300 nm) substrates (n-doped, 4–7 Ω cm), and glass substrates were cleaned by ultrasonicating in acetone, isopropyl alcohol, and double distilled water and dried under flowing N_2. The e-resist film was made by spin-coating of the Au–ToABr solution at 2000 rpm for 1 min. EBL was performed using a Nova NanoSEM 600 instrument (FEI Co., The Netherlands). The electron beam energy employed for patterning was 5 kV with a beam current of 2.9 nA. Energy dispersive X-ray spectroscopy (EDS) mapping was performed at 10 kV (energy window, 10 eV) with a beam current of 1.1 nA, the dwell time per pixel being 30 s. Thermolysis was carried out in air at 300 °C for 3 h. UV-visible spectra were recorded using a Perkin–Elmer Lambda 900 UV/visible/near-IR spectrophotometer. X-ray diffraction measurements were performed using a Bruker diffractometer (Cu Kα 1.5406 Å, scan rate, 0.5 min^{-1}). AFM measurements were done using Innova SPM with Nanodrive controller (Veeco, USA) in the contact mode. Standard Si_3N_4 cantilevers were used for the normal topography imaging. The optical images were collected using a Laben (India) microscope. For optical profilometric measurements, Wyko NT 9100 was used. Physical vapor deposition of Au contacts was done by shadow masking using a thermal evaporator (HindHivac, India) at a base pressure of 10^{-6} torr. Current–voltage measurements were done using a Keithley 236 source measure unit. For the PDMS transfer related experiments, Sylgard 184 curing agent (Dow Corning) and its elastomer were mixed in the ratio of 1:10 by weight. The mixture was then degassed under vacuum for 30 min. PDMS was poured onto nanoparticle stripes and then cured in the oven at 50 °C for 6 h. After curing, PDMS was peeled off which contained

the nanoparticle stripes. For swelling experiments, a drop of toluene was placed slightly further from the PDMS substrate at a sliding angle so as to contact the substrate.

Supporting Information

Supporting Information is available from the Wiley Online Library or from the author.

Acknowledgements

The authors thank Prof. C. N. R. Rao for his constant encouragement. Support from Department of Science and Technology, India is gratefully acknowledged. The authors acknowledge Venkatasrinu Bhadram for help with Raman measurements. B.R. thanks CSIR, India for a fellowship.

Received: December 29, 2011
Revised: February 27, 2012
Published online: April 10, 2012

[1] J. Millman, *Vacuum–Tube and Semiconductor Electronics*, McGraw–Hill, New York **1958**.
[2] B. Pradhan, S. K. Batabyal, A. Pal, *J. Appl. Phys. Lett.* **2006**, *89*, 233109.
[3] C.-H. Liu, C.-C. Wu, Z. Zhong, *Nano Lett.* **2011**, *11*, 1782.
[4] D. Dragoman, M. Dragoman, R. Plana, *J. Appl. Phys.* **2010**, *108*, 084316.
[5] I. Díez-Pérez, J. Hihath, Y. Lee, L. Yu, L. Adamska, M. A. Kozhushner, I. I. Oleynik, N. Tao, *Nat. Chem.* **2009**, *1*, 635.
[6] J. L. Dewald, W. T. Wondmagegn, A. V. Ellis, S. A. Curran, *Synth. Met.* **2005**, *155*, 39.
[7] Nourbakhsh, M. Cantoro, A. Hadipour, T. Vosch, M. H. van der Veen, M. M. Heyns, B. F. Sels, S. De Gendt, *Appl. Phys. Lett.* **2010**, *97*, 163101.
[8] C. N. R. Rao, G. U. Kulkarni, P. J. Thomas, P. P. Edwards, *Chem. Soc. Rev.* **2000**, *29*, 27.
[9] S. Chen, F. Deng, *Proc. SPIE* **2002**, *4807*, 93.
[10] S. Pal, M. K. Sanyal, N. S. John, G. U. Kulkarni, *Phys. Rev. B* **2005**, *71*, 121404.
[11] S. Chen, *Anal. Chim. Acta* **2003**, *496*, 29.
[12] V. V. Agrawal, N. Varghese, G. U. Kulkarni, C. N. R. Rao, *Langmuir* **2008**, *24*, 2494.
[13] S. A. Maier, H. A. Atwater, *J. Appl. Phys.* **2005**, *98*, 011101.
[14] While this is also true for semiconductor nanoparticles, see a) A. P. Alivisatos, *Science* **1996**, *271*, 933–937; b) A. L. Rogach, *Semiconductor Nanocrystal Quantum Dots: Synthesis, Assembly, Spectroscopy*, Springer, Austria **2008**, in this article, we restrict to metal nanoparticles.
[15] C. Salzemann, W. Zhai, N. Goubet, M.-P. Pileni, *J. Phys. Chem. Lett.* **2009**, *1*, 149.
[16] V. V. Agrawal, G. U. Kulkarni, C. N. R. Rao, *J. Phys. Chem. B* **2005**, *109*, 7300.
[17] R. L. McCreery, *Chem. Mater.* **2004**, *16*, 4477.
[18] A. Iovan, V. Korenivski, D. B. Haviland, *J. Appl. Phys.* **2006**, *99*, 08E502.
[19] P. Collier, R. J. Saykally, J. J. Shiang, S. E. Henrichs, J. R. Heath, *Science* **1997**, *277*, 1978.
[20] S. Sun, C. B. Murray, D. Weller, L. Folks, A. Moser, *Science* **2000**, *287*, 1989.
[21] C. T. Black, C. B. Murray, R. L. Sandstrom, S. Sun, *Science* **2000**, *290*, 1131.
[22] G. Markovich, C. P. Collier, S. E. Henrichs, F. Remacle, R. D. Levine, J. R. Heath, *Acc. Chem. Res.* **1999**, *32*, 415.
[23] B. Liang, X. S. Guo, J. Tu, D. Zhang, J. C. Cheng, *Nat. Mater.* **2010**, *9*, 989.
[24] S. Kinge, M. Crego-Calama, D. N. Reinhoudt, *Chem. Phys. Chem.* **2008**, *9*, 20.
[25] X. M. Lin, H. M. Jaeger, C. M. Sorensen, K. J. Klabunde, *J. Phys. Chem. B* **2001**, *105*, 3353.
[26] M. Grzelczak, J. Vermant, E. M. Furst, L. M. Liz-Marzán, *ACS Nano* **2010**, *4*, 3591.
[27] Dong, J. Chen, S. J. Oh, W.-k. Koh, F. Xiu, X. Ye, D.-K. Ko, K. L. Wang, C. R. Kagan, C. B. Murray, *Nano Lett.* **2011**, *11*, 841.
[28] G. C. Jensen, C. E. Krause, G. A. Sotzing, J. F. Rusling, *Phys. Chem. Chem. Phys.* **2011**, *13*, 4888.
[29] W. Cheng, N. Park, M. T. Walter, M. R. Hartman, D. Luo, *Nat. Nanotechnol.* **2008**, *3*, 682.
[30] B. Radha, G. U. Kulkarni, *Nano Res.* **2010**, *3*, 537.
[31] P. J. Thomas, G. U. Kulkarni, C. N. R. Rao, *J. Mater. Chem.* **2004**, *14*, 625.
[32] B. J. Y. Tan, C. H. Sow, T. S. Koh, K. C. Chin, A. T. S. Wee, C. K. Ong, *J. Phys. Chem. B* **2005**, *109*, 11100.
[33] S.-H. Yun, S. I. Yoo, J. C. Jung, W.-C. Zin, B.-H. Sohn, *Chem. Mater.* **2006**, *18*, 5646.
[34] B. Radha, A. A. Sagade, G. U. Kulkarni, *ACS Appl. Mater. Interface* **2011**, *3*, 2173.
[35] M. K. Corbierre, J. Beerens, R. B. Lennox, *Chem. Mater.* **2005**, *17*, 5774.
[36] R. Glass, M. Arnold, J. Blümmel, A. Küller, M. Möller, J. P. Spatz, *Adv. Funct. Mater.* **2003**, *13*, 569.
[37] B. Radha, S. Kiruthika, G. U. Kulkarni, *J. Am. Chem. Soc.* **2011**, *133*, 12706.
[38] K.-C. Kim, I.-B. Lee, D.-J. Kang, S. Maeng, *Etri J.* **2007**, *29*, 814.
[39] J. Marqués-Hueso, R. Abargues, J. Canet-Ferrer, S. Agouram, J. L. Valdés, J. P. Martínez-Pastor, *Langmuir* **2009**, *26*, 2825.
[40] J. K. W. Yang, K. K. Berggren. *J. Vac. Sci. Technol. B* **2007**, *25*, 2025.
[41] J. Robertson, *Mater. Sci. Eng. R.* **2002**, *37*, 129.
[42] B. Radha, M. Arif, R. Datta, T. K. Kundu, G. U. Kulkarni, *Nano Res.* **2010**, *3*, 738.
[43] M. Yasuda, H. Kawata, K. Murata, K. Hashimoto, Y. Hirai, N. Nomura, *J. Vac. Sci. Technol. B* **1994**, *12*, 1362.
[44] Z. Cui, *J. Phys. D* **1992**, *25*, 919.
[45] Silicon- Wikipedia, the free encyclopedia, http://en.wikipedia.org/wiki/Silicon, (February, 2012).
[46] K. Yasuhiko, K. Takahisa, *Nanotechnology* **2008**, *19*, 255605.
[47] S. Herminghaus, K. Jacobs, K. Mecke, J. Bischof, A. Fery, M. I. Elhaj, S. Schlagowski, *Science* **1998**, *282*, 916.
[48] G. J. Ashwell, W. D. Tyrrell, A. J. Whittam, *J. Mater. Chem.* **2003**, *13*, 2855.
[49] G. J. Ashwell, A. Mohib, *J. Am. Chem. Soc.* **2005**, *127*, 16238.
[50] C. C. Bof Bufon, J. D. Arias Espinoza, D. J. Thurmer, M. Bauer, C. Deneke, U. Zschieschang, H. Klauk, O. G. Schmidt, *Nano Lett.* **2011**, *11*, 3727.
[51] J. M. Beebe, B. Kim, J. W. Gadzuk, C. Daniel Frisbie, J. G. Kushmerick, *Phys. Rev. Lett.* **2006**, *97*, 026801.
[52] T. I. Kim, J.-h. Kim, S. J. Son, S. M. Seo, *Nanotechnology* **2008**, *19*, 295302.
[53] L. Hong, L. Huiqin, L. Ming, M. Dali, *ICEPT*, **2007**, 1.
[54] C. Dong-Uk, S. Kumar, K. Gil-Ho, *IEEE–Nano* **2009**, 261.
[55] D. I. Son, D. H. Park, J. B. Kim, J.-W. Choi, T. W. Kim, B. Angadi, Y. Yi, W. K. Choi, *J. Phys. Chem. C* **2011**, *115*, 2341.
[56] C. H. Lee, D. R. Kim, X. Zheng, *Proc. Natl. Acad. Sci. USA* **2010**, *107*, 9950.
[57] C. Moraes, Y. Sun, C. A. Simmons, *J. Micromech. Microeng.* **2009**, *19*, 065015.
[58] J. N. Lee, C. Park, G. M. Whitesides, *Anal. Chem.* **2003**, *75*, 6544.
[59] M. Brust, M. Walker, D. Bethell, D. J. Schiffrin, R. J. Whyman, Chem. *Soc. Chem. Commun.* **1994**, *7*, 801.